Journal of
Nanoscience and Nanotechnology
Vol. 5, 334–345, 2005

RESEARCH ARTICLE

Microscopy and Quantitative Morphology of Aluminum Silicate Nanoparticles Grown on Organic Templates

Bongwoo Kang,[1] Giovanni F. Crosta,[1,2,*] Peter J. Stenhouse,[3] and Changmo Sung[2]

[1] *Center for Advanced Materials, University of Massachusetts, Lowell, Massachusetts, USA*
[2] *Department of Environmental Sciences, Università degli Studi Milano—Bicocca, 1, Piazza della Scienza, I 20126 Milan, Italy*
[3] *US Army Natick Soldier Center, Natick, Massachusetts, USA*

Biomimetic synthesis of ceramic materials is increasing in popularity because it offers many advantages. In this work, aluminum silicate nanoparticles were obtained on a self-assembled organic multilayer at near room temperature ($30 \leq T \leq 50$ °C) and at atmospheric pressure. Morphological and microanalytical characterization was carried out by means of transmission electron microscopy and subsequent image analysis. The roles of some process parameters such as template type, reactant concentration, [Al]:[Si] molar ratio, number of initiation steps (IS) of mineralization, and reaction time (rt) were assessed by comparing images, diffraction patterns, and EDX spectra. Generally, the Si-rich phase exhibited higher crystallinity, whereas the Al-rich phase was mostly amorphous. Crystal structure resulted with rt $\geq$ 4 days for template-grown materials. Images of materials obtained at $T = 50$ °C, rt = 3 days, and $1 \leq$ IS ≤ 4 were further analyzed by "spectrum enhancement," an algorithm based on the Fourier transform. Morphological indicators were extracted from suitably processed power spectral densities, a correlation matrix was formed, and multivariate statistics was carried out. Visual differences in nanoaggregate morphology were quantitatively translated. Materials were ranked by the spatial uniformity of nanoparticle distribution: the most uniform aggregates were those grown on templates by IS ≥ 2. Univariate statistics validated the conclusion: the particles of those same materials had a narrower size distribution and sharper edges. This last property has been ascribed to crystalline structure, independently demonstrated by diffraction patterns.

Keywords: Biomimetic Synthesis, Image Classification, Morphological Descriptors.

1. INTRODUCTION

The production of inorganic crystals grown on organic templates to a specific design is desirable for material processing since crystallographic selectivity determines the physical properties of the inorganic phase. The manufacture of ceramics generally involves very high temperatures and pressures and the use of toxic organic solvents. For example, the traditional approach to producing aluminosilicate materials is based on the synthesis of ceramic powder from precursor materials, followed by pressureless sintering above 1650 °C, hot pressing at above 1500 °C, or, in the best situation, sintering at $1000 \leq T \leq 1250$ °C.

In the self-assembly approach, instead, physical interaction between the precursor materials and specific molecules deposited on the surface of a solid substrate promotes the formation of stable, organized films on the substrate[1,2] at near room temperature. Preparation of the substrate requires layer-by-layer deposition of charged polymers controlled by electrostatic forces: this technique has been introduced and successfully applied to the synthesis of various compounds such as polymer–polymer, polymer–organic, polymer–inorganic, and polymer–mineral compositions, electroactive rod-like polymers and polymer–biomolecule systems.[3,4] The

*Author to whom correspondence should be addressed.

 1533-4880/2005/5/334/012/$17.00+.25 doi:10.1166/jnn.2005.029

potential applications of this technique include thin films and coatings such as heat sinks, scratch-resistant coatings, magnetic recording heads, ultraviolet blockers, and medical implants.

This work deals with nanoaggregates of aluminum silicate particles grown on an organic template at atmospheric pressure and near room temperature. In order to assess the role of some control parameters in the mineralization process, the morphological, microstructural, and microanalytical properties of the materials are investigated.

Images and data have been obtained by TEM (transmission electron microscopy), selected area diffraction patterns (SADP), and EDXS (energy dispersive X-ray spectrometry). Morphology has been quantitatively analyzed and classified by Fourier methods followed by multivariate statistics.

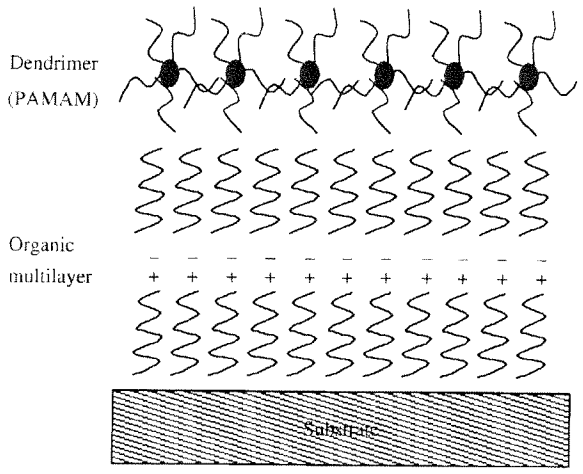

Fig. 1. Pictorial representation of a self-assembled organic multilayer template.

2. EXPERIMENTAL PROCEDURES AND EXPERIMENT DESIGN

2.1. Formation of the Polymer Multilayer

The substrates for the formation of ceramic particles were 200-mesh Formvar™ copper grids coated by an amorphous carbon film, commonly used as TEM specimen holders.

The self-assembled organic template was formed stepwise: first, a layer of positively charged *d*-PDAC [poly(diallyldimethylammonium chloride)] was deposited on the TEM grid, which was then rinsed with deionized water and allowed to dry for a few minutes at room temperature. Next the grid was immersed in a solution of *d*-polyphenol red + polyaniline, from which a negatively charged layer was formed by self-assembly. The grid was again rinsed and dried. The sequence was repeated for a few times. Some of the dry multilayered grids were immersed in a 10.3 wt % solution of sulfonate-terminated PAMAM (polyamidoamine) dendrimer.[5] The sample surface was eventually rinsed and dried.

A self-assembled organic multilayer template is depicted in Figure 1.

2.2. Design of the Mineralization Experiment

Basically, mineralization consisted of immersing the grid in a nonaqueous solution of the reactants at a given temperature and adding a fixed amount of water either in a single dose, i.e., in one "initiation step," or divided into more steps and letting the reaction proceed for some time. The reactants were aluminum isopropoxide ($Al(OiPr)_3$) and tetraethylorthosilicate ($Si(OEt)_4$) and the solvent was *tert*-butyl alcohol. The experimental control parameters and the respective ranges of values were the following.

- substrate type: plain TEM grid or template with or without PAMAM
- solution concentration, c: 10 mM $\leq c \leq$ 100 mM
- $[Al(OiPr)_3]$ to $[Si(OEt)_4]$ molar ratio, [Al]:[Si]: 1:3 $\leq$ [Al]:[Si] $\leq$ 3:1
- reaction temperature, T: 30 $\leq T \leq$ 50 °C
- reaction time, rt: 8 h $\leq$ rt $\leq$ 7 days
- number of initiation steps, IS: 1 $\leq$ IS $\leq$ 4

Several sets of samples were prepared with different combinations of the control parameters, the purpose being to assess the role of each parameter in the properties of the end product. Among them the C ("coated") and U ("uncoated") sets, studied in Sections 4 and 5, were such that $c = 50$ mM, [Al]:[Si] = 1:3, $T = 50$ °C, and rt = 3 days. The C samples were mineralized on organic templates, those of U were mineralized on plain grids to serve as negative control. In particular, the samples C1 and C2 were obtained by IS = 4, C3 by IS = 3, C4 by IS = 2, and C5 and C6 by IS = 1. Similarly, IS = 4 for U1 and so forth up to U5 (U6 had to be discarded because of contamination during the experiment).

Further details of multilayer substrate preparation and specimen formation are reported in Ref. 6.

2.3. TEM Characterization

Grids were examined by a Philips EM 400t fitted with LaB_6 filament at 120 keV. To minimize radiation damage on samples the electron beam intensity was kept as low as possible. Electron diffraction patterns were obtained by selected area or convergent beam diffraction method. Dark field images of crystalline grains were also acquired from (*hkl*) diffraction spots in SADPs. The Noran-EDAX ultrathin window detector was used with an electron probe size ranging from 20 to 60 nm for elemental microanalysis.

RESEARCH ARTICLE

3. MICROSTRUCTURAL AND MICROANALYTICAL RESULTS: THE ROLE OF PROCESS PARAMETERS ON MORPHOLOGY AND CRYSTAL STRUCTURE

3.1. Role of the Template

The expected role of the organic template was to promote and control the formation of aluminum silicate nanoparticles. Figure 2 shows both TEM images and SADPs of materials grown on plain grids (A) and with a template (B).

In the first place, nanoparticles of A specimens were difficult to locate, whereas the density and uniformity of particles grown on the multilayer template (B) were dramatically increased. Moreover the template was found to be necessary to produce crystalline nanoparticles in a reliable way. The peaks in the right (B) SADP of Figure 2 provide the evidence.

Mineralization on PAMAM dendrimer at rt = 4 days yielded aluminum oxide.

The role of the template is further discussed in Sections 5.2 and 5.3.

3.2. Role of Reactant Concentration

The role of reactant concentration on template-grown specimens is illustrated by Figure 3. As c was increased from 10 to 20 mM, the remaining parameters being fixed, crystallinity and particle density increased. As expected, the reaction from a more concentrated solution had a higher yield.

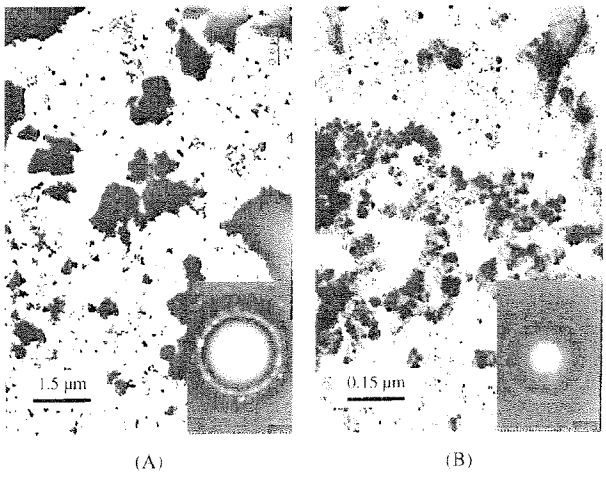

Fig. 2. TEM images (top) and electron diffraction pattern (bottom) of aluminum silicate nanoparticles grown on a plain grid (A) and on a template (B). $c = 10$ mM, [Al]:[Si] = 1:3, $T = 50$ °C, rt = 4 days. Same IS. Note the different scale.

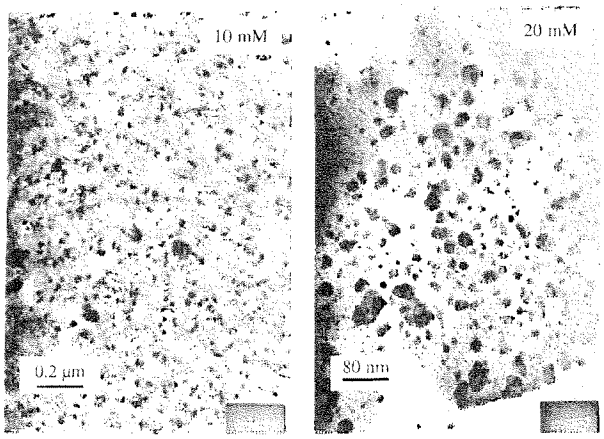

Fig. 3. TEM images of crystalline aluminum silicate nanoparticles obtained with $c = 10$ mM (left) and $c = 20$ mM (right). rt = 3 days. Same T and IS. Note the different scale.

3.3. Role of Reaction Time

The minimum rt necessary to produce nanosized particles (<15 nm) of aluminum silicate was found to be 8 h. With rt $\leq$ 3 days no peaks were recorded in any SADP, whereas with rt $\geq$ 4 days peaks were visible in template-grown materials (Fig. 2B). When rt was increased to 7 days, the result shown in Figure 4 was obtained. Nanoparticles were well-developed, uniformly distributed over the substrate surface, and crystalline. From the TEM picture one can also deduce that the particle density was high.

3.4. Role of Si Molar Ratio

As the [Al]:[Si] ratio in the solution was decreased, the particles did exhibit a higher Si concentration. Materials produced at [Al]:[Si] ratios of 3:1 and 1:3 have also been compared.

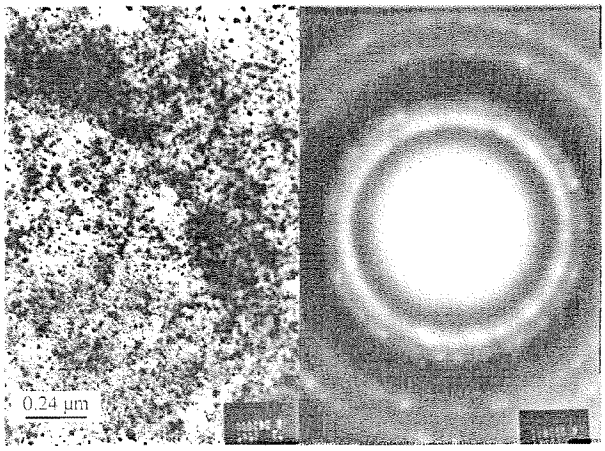

Fig. 4. TEM image and electron diffraction from the longest rt (=7 days).

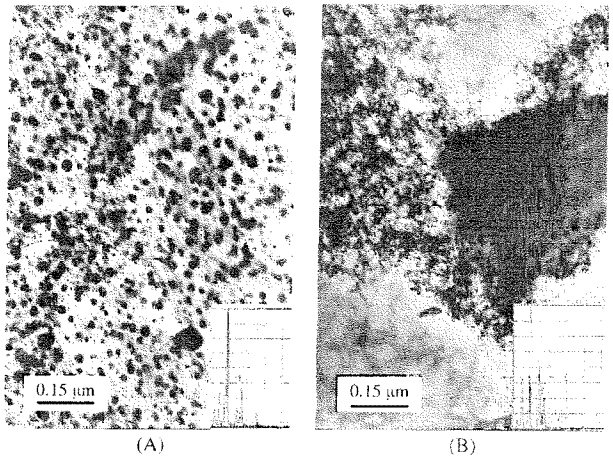

Fig. 5. TEM images and EDX spectra of Si rich phase (A) and Al rich phase (B). rt = 7 days. IS = 3.

The images and EDX spectra of Figure 5 pertain to the Si-rich phase (A) and to the Al-rich phase (B). The former exhibited higher crystallinity, whereas the latter was mostly amorphous.

4. METHODS OF IMAGE ANALYSIS AND MATERIALS CLASSIFICATION

Sets of TEM images of the materials C1–C6 and U1–U5 were obtained at various magnifications including 130 K× and 280 K×. Positive photographic plates were digitized and stored as files in JPEG format, then converted into the grayscale Sun raster™ format such that the 0 gray level corresponded to black and 255 to white. The approximate size of the resulting image (parent image) was 1250 × 1100 pixels. Image processing relied on the discrete Fourier transform, therefore tiles of 512^2 pixels had to be cut out of parent images. Typically 6 tiles were obtained, which covered the whole area of the parent image with partial overlap. A sample tile of material C1 at 130 k× is shown in Figure 6. Qualitatively, morphology is similar to that of a hybrid Mullite gel heated at 1000 °C shown in Figure 7 of Ref. 7.

Notation: tiles from a given parent image of a given material form a level 1 class. Tiles from different parent images but from the same material form level 2 classes. Finally, level 3 classes are made of tiles having only the IS parameter in common.

The purpose of image analysis was threefold and had to be carried out at three levels according to the following design.

- At levels 1 and 2 (given material, IS, and magnification), quantify the spatial uniformity of nanoparticle distribution and morphology.
- At level 3 (given IS and magnification), compare the morphologies of materials grown on coated (C) or on uncoated (U) grids.

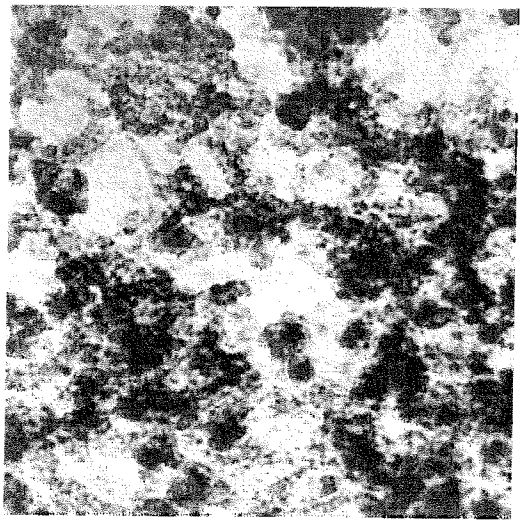

Fig. 6. Grayscale image of material C1, tiles 1–501. Magnification = 130 K×. Square side length = 290 nm.

- At *given magnification*, attempt material classification by means of morphological descriptors.

As it will be explained below, the goals have been achieved by means of Fourier analysis followed by the extraction of morphological descriptors and multivariate statistics.

4.1. Fourier Analysis and Spectrum Enhancement

Although image processing was carried out on a digital image defined in a discrete domain, the definition and properties of "spectrum enhancement" are best described in the continuum setting.

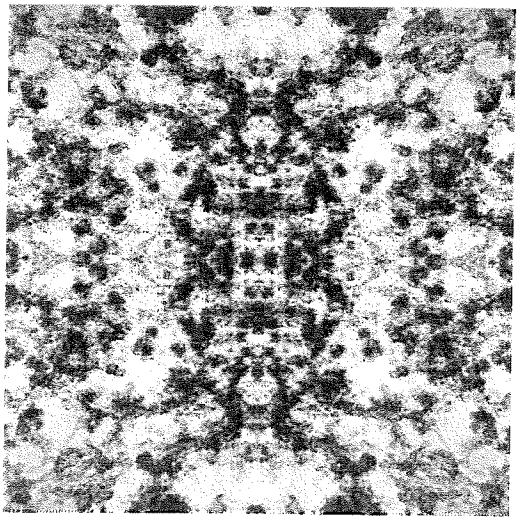

Fig. 7. Flip-flopped tile of Figure 6. Square side length = 580 nm.

Let the image be represented by a nonnegative function $g[\boldsymbol{x}]$ of position $\boldsymbol{x}$ belonging to the domain Ω, which corresponds to a tile. Let $Q[\cdot]$ denote the twofold flop[flip[$\cdot$]] reflection. The domain $Q\Omega$ is a square of area 4 times that of Ω and is locally isomorphic to (is a geographic map of) the surface $\mathcal{T}$ of a torus. The flop-flipped function $Q[g]$ is continuous on $\mathcal{T}$. In other words, it has spatial period $Q\Omega$. An example is shown by Figure 7.

Let the Fourier transform $G[\cdot]$ of $Q[g[\cdot]]$ exist. Then $G[\cdot]$ is a function of the spatial frequency vector $\boldsymbol{u} \equiv \{u_1, u_2\}$. Polar coordinates $\boldsymbol{u} \equiv \{u, \vartheta\}$, where $u := |\boldsymbol{u}|$ is wavenumber and ϑ the polar angle, are more conveniently used. Let L be the side length of $Q\Omega$ and ℓ be the pixel side length. If the value of the function $Q[g[\cdot]]$ is assigned at the center of each pixel, then $Q[g[\cdot]]$ admits a Fourier transform defined at discrete spatial frequencies which vary in the interval

$$0 \le |u_1|, |u_2| \le u_{\max} = \frac{L}{2\ell} - 1$$

For example, if $L = 1$ and the grid laid over $Q\Omega$ has 1024^2 pixels, then $\ell = 1/1024$ and $\frac{L}{2\ell} = 512$ cycles/image. At the magnification of 130×, 511 cycles/image correspond to 881 cycles μm^{-1}.

One may note that, as a consequence of flip-flopping, $G[\cdot]$ is free from the "cross artifact." Figure 8 displays the power spectral density $|G[u, q]|^2$ obtained from Figure 7.

By averaging the logarithm of $|G[u, \vartheta]|^2$ over an arc Θ, the dependence on ϑ was removed and the following function of u alone was obtained

$$s[u] = \frac{1}{|\Theta|} \int_{\Theta} 10\,\mathrm{Log}[|G[u, \vartheta]|^2] u\, d\vartheta - 10\,\mathrm{Log}[|G[\mathbf{0}]|^2]$$

where $|\Theta| = 2u\delta$ is arc length. In the applications below $\delta = \frac{\pi}{2}$, hence $-\frac{\pi}{2} \le \vartheta \le \frac{\pi}{2}$ and $|\Theta| = u\pi$. Angle averaging smoothed out the ϑ-dependent oscillations of $\mathrm{Log}[|G[u, \vartheta]|^2]$. It also removed information about the possible anisotropy of the material.

Next a model power spectral density, $m^{(p)}[u]$, was introduced according to

$$m^{(p)}[0] = 0; \quad m^{(p)}[u] = -10\,\mathrm{Log}[u^{(p)}], \quad u \ge 1$$

The exponent p characterizes the model. Values of p ranging from 1.4 to 3.6 were used, as described below. Subtraction of the model from the angle-averaged spectrum yielded the enhanced spectrum $h[u]$

$$h^{(p)}[u] = s[u] - m^{(p)}[u], \quad 0 \le u \le 511 \text{ cycles/image}$$

The idea behind choosing $h^{(p)}[u]$ was precisely to enhance the deviations of $s[u]$ from a reference spectral density, the model $m^{(p)}[\cdot]$. The enhanced spectrum derived from Figure 6 is the sequence of filled boxes in Figure 9. The meaning of spectrum enhancement is further explained in the Discussion (Section 6). More properties and applications of spectrum enhancement to image classification can be found in Refs. 8 and 9.

4.2. Extraction of Morphological Descriptors

The enhanced spectrum of a flop-flipped tile was the set of "raw data" from which two types of morphological descriptors were extracted.

- Type 1: the graph of the interpolating polynomial $q^{(p,d)}[\cdot]$ of sufficiently high degree d (=14 in this paper),
- Type 2: some properties of the polynomial such as the abscissa and ordinate of the proper maximum and so forth.

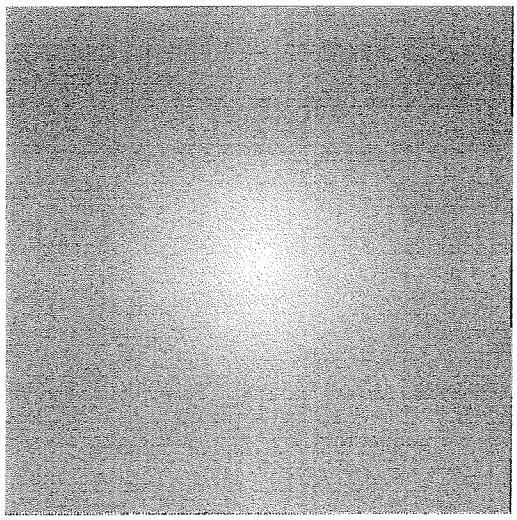

Fig. 8. Normalized power spectral density obtained from Figure 7. Origin of the reciprocal plane $\{u_1, u_2\}$ at the center of the square. Range: $0 \le |u_1|, |u_2| \le 511$ cycles/image.

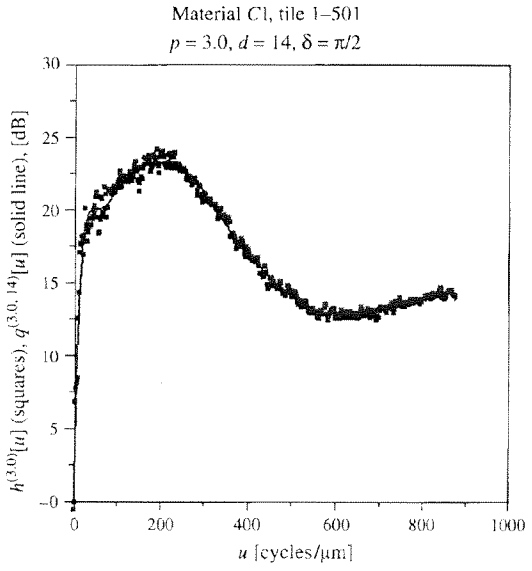

Fig. 9. Enhanced spectral density $h^{(3.0)}[u]$ of tile 1–501 and interpolating polynomial $q^{(3.0, 14)}[u]$. Spatial frequency in cycles μm^{-1} such that 511 cycles/image = 881 cycles μm^{-1}.

The solid line in Figure 9 represents the $q^{(p,d)}[\cdot]$ obtained from $h^{(p)}[\cdot]$, where $p = 3.0$, $d = 14$.

4.3. Supervised Statistical Classification

Multivariate statistics was based on the analysis of mean-removed polynomials, defined by $q_j^{(p,d)}[\cdot] - \langle q_j^{(p,d)} \rangle$, where j is the tile label and $\langle q_j^{(p,d)} \rangle$ the mean of $q_j^{(p,d)}[\cdot]$. The empirical covariance matrix was formed, and then, by normalization, the correlation matrix $\boldsymbol{R}^{(p,d)} = [R_{i,j}^{(p,d)}]$ was obtained.

The entry $R_{i,j}^{(p,d)}$ is an indicator of similarity between the enhanced spectra of tile i and tile j at fixed p and d. Namely, $R_{i,j}^{(p,d)}$ close to $+1$ means that the graphs of the (mean removed) polynomials $q_i^{(p,d)}[\cdot]$ and $q_j^{(p,d)}[\cdot]$ almost overlap, whereas $|R_{i,j}^{(p,d)}| \cong 0$ means lack of any resemblance (orthogonality). Finally, $R_{i,j}^{(p,d)}$ close to -1 means resemblance between $q_i^{(p,d)}[\cdot]$ and $-q_j^{(p,d)}[\cdot]$.

Scattergrams i.e., pictorial representations of $\boldsymbol{R}^{(p,d)}$ where the values of $R_{i,j}^{(p,d)}$ are coded by gray levels, are shown in Figures 10 and 11. Black corresponds to the value of $\min R_{i,j}^{(p,d)}$ (shown in each figure) and white to the value of $\max R_{i,j}^{(p,d)}$ (=1). Note that the main diagonal goes from the bottom left to the top right vertex. The figures describe sets 90 and 40 respectively.

Tile indices were ordered by material (for example, $1 \leq i \leq 6$ corresponds to tiles of material C1 in Fig. 10), hence the blocks along the main diagonal of $\boldsymbol{R}^{(p,d)}$ represented level 1 classes. At the next aggregation level contiguous diagonal superblocks represented level 2 classes of given substrate type and *IS* but different parent images or experiment (for example, the superblock $1 \leq i, j \leq 12$ in Fig. 10

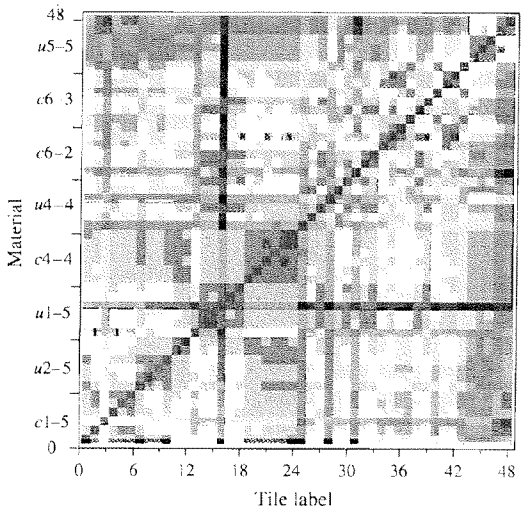

Fig. 10. Scattergram of set 90 (48 tiles). Magnification = 130 K×, $p = 3.0$, $d = 14$, $\mu^{(3.0,14)} = -0.014863$. Grayscale min = −0.014 863 (black), max = 1.0 (white). Material C4 corresponds to the light gray block at $19 \leq i, j \leq 24$, the outlier tile of material U1 to the black stripes at $i = j = 16$.

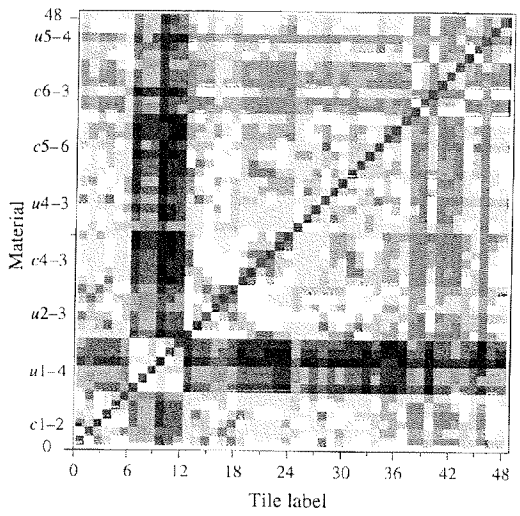

Fig. 11. Scattergram of set 40. Magnification = 280 K×, $p = 2.7$, $d = 14$, $\mu^{(2.7,14)} = 0.016429$. Grayscale min = 0.016429 (black), max = 1.0 (white). Material C4 stands out for the lightest block at $19 \leq i, j \leq 24$. Material U1 is the least correlated to the rest (dark stripes at $7 \leq j \leq 12$, $i \neq j$, and $7 \leq i \leq 12$, $j \neq i$).

corresponds to tiles of materials C1 and C2 both template grown and having IS = 4). The largest superblocks represented level 3 classes having the same IS, regardless of coating (for example, $1 \leq i, j \leq 18$ in Fig. 10 corresponds to tiles of the three materials C1, C2 and U1).

The two following indicators were chosen:

- $\mu^{(p,d)} = \min_{i,j} R_{i,j}^{(p,d)}$, the array-wide minimum cross correlation (coded by black in the figures), to represent overall inter-class heterogeneity; intuitively, the lower $\mu^{(p,d)}$, the higher the heterogeneity;
- $\beta_B^{(p,d)} = \min_{i,j \in B} R_{i,j}^{(p,d)}$, where B is the set of indices which form a block of $\boldsymbol{R}^{(p,d)}$, to represent intra-class homogeneity for each class. Intuitively, the higher the $\beta_B^{(p,d)}$, the more homogeneous the class.

Univariate statistics was based on type 2 morphological descriptors, some of which have been listed above. Details will be discussed in Sections 5.4 and 6.

The spectrum enhancement code was based on fast Fourier transform and singular value decomposition taken from Ref. 10 and on additional feature extraction functions. It was written in *c* and compiled by *xlc* or *gcc* on some IBM RS/6000 42t machines. Other software tools were ImageMagick® 4.2.8 for IBM AIX® 4.1 and Spyglass Plot®.

5. MATERIAL CLASSIFICATION RESULTS

Morphological analysis was carried out on the sets listed in Table I. The value of d was kept fixed (=14), whereas that of p was made to vary from 1.4 to 3.6 in steps of 0.2 or 0.1. Classification was of supervised type because the origin of each tile was known beforehand.

RESEARCH ARTICLE

Table I. Image sets.

Material name	Template	IS	Tile no. range in set 90 130× Figure 10	Tile no. range in set 40 280× Figure 11
C1	Y	4	1–6	1–6
C2	Y	4	7–12	—
C4	Y	2	19–24	19–24
C5	Y	1	—	31–36
C6	Y	1	31–42	37–42
U1	N	4	13–18	7–12
U2	N	4	—	13–18
U4	N	2	25–30	25–30
U5	N	1	43–48	43–48

5.1. Choice of the Model Exponent p

In general the entries of $R^{(p,d)}$ and all derived indicators exhibit dependence on p and d. As a consequence, all conclusions of morphological analysis may seem to follow from the arbitrariness of these parameters. However, if there exists at given d an interval of p within which some indicator is less sensitive to p, then results express the properties of the analyzed materials, almost independently of the model. The most straightforward property which characterizes the materials is interclass heterogeneity, expressed by $\mu^{(p,14)}$. Generally, $\mu^{(p,14)} > 0.6$, i.e., a too high minimum means that the given model poorly discriminates classes. If $\mu^{(p,14)} < 0.6$, no conclusion can be drawn.

As p was increased, $\mu^{(p,14)}$ had a decreasing trend, regardless of magnification (130× or 280×). For the set 90 $\mu^{(p,14)}$ was found to depend on p as summarized by Table II. In the interval $2.9 \leq p \leq 3.3$, $\mu^{(p,14)}$ was the least sensitive to p and at the same time its magnitude was closest to 0. More precisely, a local minimum of $\mu^{(p,14)}$ occurred at $p = 3.0$ and a local maximum at $p = 3.2$, both shown in boldface in Table II. To simplify the analysis, both C1 and C2 were assigned to the same level 2 classes (coated substrate, IS = 4). The following saddle point problem had to be solved:

> "find $\hat{p}$ which at the same time maximizes interclass heterogeneity (minimum $\mu^{(p,14)}$) and minimizes the heterogeneity within each class (namely, the $\beta_B^{(p,14)}$'s, for all diagonal blocks B, are local maxima)."

The solution was $\hat{p} = 3.0$. These results indicated that intrinsic morphological properties of the set could be sorted out.

The situation of set 40 is summarized by Table III. Values of $\mu^{(p,14)}$ also decreased with increasing p. A local minimum occurred at $p = 3.4$ and a local maximum at $p = 3.6$. However, both $|\mu^{(3.4,14)}|$ and $|\mu^{(3.6,14)}|$ were significantly greater than 0. Both values were disregarded in favor of $\hat{p} = 2.7$, where $|\mu^{(2.7,14)}| = 0.0164$, shown in boldface in Table III.

Table II. Dependence on p of overall interclass heterogeneity $\mu^{(p,14)}$ for set 90.

p	$\mu^{(p,14)}$	Material pairs
1.4	0.67	C1, U5
1.6	0.74	U1, C6
1.8	0.68	U1, C4
2.0	0.61	C1, U1
2.2	0.62	U1, U4
2.4	0.55	U1, U4
2.6	0.46	U1, U4
2.8	0.16	U1, U5
3.0	**−0.01**	U1, U5
3.2	**0.06**	U1, U5
3.4	−0.22	U1, U5
3.6	−0.28	U1, U5

The values of $\mu^{(p,14)}$ which are least sensitive to p are shown in boldface. The chosen exponent is $\hat{p} = 3.0$. At fixed p the minimum of $\mu^{(p,14)}$ (highest heterogeneity) is attained at the material pairs shown in the 3rd column.

5.2. Spatial Uniformity of Nanoparticle Distribution and Morphology

This property is expressed by intraclass homogeneity, $\beta_B^{(p,d)}$. The results of Figure 10 and Table IV were obtained from set 90 at $\hat{p} = 3.0$, $d = 14$, whereas Figure 11 and Table V were derived from set 40 at $\hat{p} = 2.7$, $d = 14$.

Set 90

With reference to column 4 of Table IV, the most homogeneous level 1 class of this set was C4 with $\beta_B^{(3.0,14)} = 0.9122$. This corresponds to the highest spatial uniformity. The level 2 class {C1, C2} was the next best. Both values of $\beta_B^{(3.0,14)}$ are shown in boldface.

Table III. Dependence on p of overall interclass heterogeneity $\mu^{(p,14)}$ for set 40.

p	$\mu^{(p,14)}$	Material pairs
1.6	0.59	U1, C4
1.8	0.52	U1, C4
2.0	0.39	U1, C4
2.2	0.35	U1, C4
2.4	0.25	C5, U1
2.6	0.09	C5, U1
2.7	**0.02**	C5, U1
2.8	−0.07	C5, U1
3.0	−0.12	C4, U1
3.2	−0.24	C4, U1
3.4	−0.38	C4, U1
3.6	−0.25	C5, U1

The value of $\mu^{(p,14)}$ which is least sensitive to p is shown in boldface. The chosen exponent is $\hat{p} = 2.7$ (see text). At fixed p the minimum of $\mu^{(p,14)}$ (highest heterogeneity) is attained at the material pairs shown in the 3rd column.

Table IV. Spatial uniformity indicators for set 90 and role of template growth.

			$\beta_B^{(3.0,14)}$	
IS	Template	Materials	Level 2 class	Level 3 class
1	Y	C6	0.5951	0.1504
	N	U5	0.6657	
2	Y	C4	**0.9122**	*0.5433*
	N	U4	*0.5433*	
3	Y	C3	N.A.	N.A.
	N	U3	N.A.	
4	Y	C1	**0.7197**	*0.2129*
		C2		
	N	U1	*0.2129*	

$p = 3.0$, $d = 14$.
Boldface entries designate materials for which template growth improved uniformity at fixed IS.

Material ranking by uniformity, denoted by "$\succ$," was

$$C4 \succ \{C1, C2\} \succ U5 \succ C6 \succ U4 \succ U1$$

In other words, among materials grown on a template, the best result seems to have been obtained with IS = 2.

Since the C4 level 1 class was such that $\beta_B^{(p,14)} > 0.779$ in the relatively wide interval $1.4 \leq p \leq 3.6$, one concluded that spatial uniformity is an intrinsic property of the C4 material.

The other extreme behavior, i.e., the lowest uniformity, was exhibited by level 1 class U1, which contained an "outlier" tile, represented by the two black stripes at $i = 16$, $j = 16$ in Figure 10 and became uncorrelated at $p = 3.6$. Namely $\beta_B^{(3.6,14)} = -0.063$.

Ranking derived from Table IV has a qualitative counterpart in the grayscale levels of blocks in Figure 10. The C4 block, $19 \leq i, j \leq 24$, stands out for its uniform gray level and the high values of $R_{i,j}^{(3.0,14)}$. The U4 block, $25 \leq i, j \leq 30$, instead, has fewer high correlation entries besides those on the main diagonal. Similar properties can be observed in the {C1, C2} and the C6 blocks.

Set 40

On the finer scale, the smaller $\beta_B^{(p,14)}$'s in column 4 of Table V and the higher count of dark pixels in Figure 11 suggest a higher intraclass heterogeneity. This is a predictable consequence of higher magnification.

Nonetheless, material C4 continued to be the most spatially uniform: $\beta_B^{(p,14)} > 0.62$ in the interval $2.5 \leq p \leq 3.0$, inside which $|\mu^{(p,14)}| < 0.15$, i.e., overall heterogeneity was the highest.

At $\hat{p} = 2.7$, materials were ranked by uniformity as follows:

$$C4 \succ U2 \succ U1 \succ C1 \succ U4 \succ C5 \succ U5 \succ C6.$$

5.3. Role of the Template: Comparison between Materials Grown on Coated vs Uncoated Grids

The findings of Section 3.1 found a counterpart in quantitative morphology. More precisely, the role of the template in controlling uniformity of the nanomaterial was assessed by comparing $\beta_B^{(p,d)}$ at levels 2 and 3. At level 2 substrate properties are taken into account (columns 4 of Tables IV and V), whereas at level 3 the substrate type is disregarded (columns 5 of Tables IV and V).

With reference to material set 90 at $\hat{p} = 3.0$, one deduces the following.

IS = 2

Level 2: templates did improve spatial uniformity. Indeed, at IS = 2 class C4 is highly homogeneous ($\beta_B^{(3.0,14)} = 0.9122$), whereas class U4 is not ($\beta_B^{(3.0,14)} = 0.5433$, block $25 \leq i, j \leq 30$ of Fig. 10).

Level 3: Forming the class {C4, U4} does not further decrease homogeneity. One still has $\beta_B^{(3.0,14)} = 0.5433$ (italicized in column 5 of Table IV). In other words, the intrinsic inhomogeneity of (level 2) class U4 dominates even in the enlarged set formed by C4 and U4 together (block $19 \leq i, j \leq 30$ of Fig. 10).

To further illustrate the claim, the mean removed polynomials $q^{(3.0,14)}[\cdot] - \langle q_j^{(3.0,14)} \rangle$ of the level 1 classes C4 and U4 (set 90) have been plotted in Figures 12 and 13.

IS = 4

The same property continues to hold, i.e., when class U1 is enlarged to {C1, C2, U1}, in the block $1 \leq i, j \leq 18$ of Figure 10, which contains the black stripes $\{i = 16, i \neq j\}$ and $\{j = 16, j \neq i\}$, the homogeneity index is $\beta_B^{(3.0,14)} = 0.2129$.

IS = 1

Different properties become apparent.

Table V. Spatial uniformity indicators for set 40 and role of template growth.

			$\beta_B^{(2.7,14)}$	
IS	Template	Materials	Level 2 class	Level 3 class
1	Y	C5	0.485	0.389
		C6		
	N	U5	0.4921	
2	Y	C4	**0.7855**	0.641
	N	U4	0.7089	
3	Y	C3	N.A.	N.A.
	N	U3	N.A.	
4	Y	C1	**0.7265**	0.133
	N	U1	0.133	
		U2		

$\hat{p} = 2.7$, $d = 14$.
Boldface entries designate materials for which template growth improved uniformity at fixed IS.

RESEARCH ARTICLE

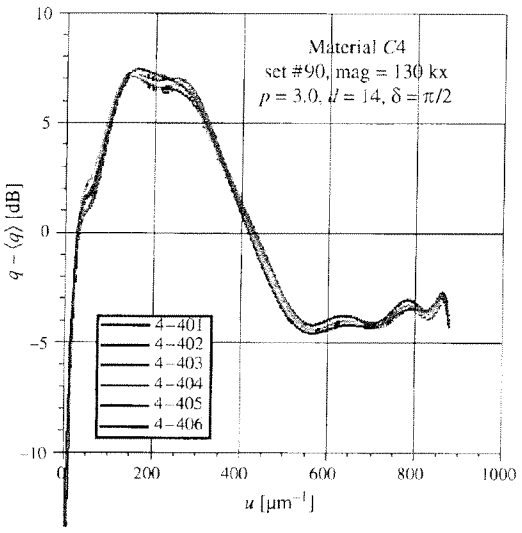

Fig. 12. Mean removed polynomials of level 1 class C4. Set 90. Spatial uniformity over the whole area (720 nm × 540 nm) is inferred from the overlap of the curves. The corresponding block in Figure 10 is $19 \leq i, j \leq 24$.

Homogeneity of the level 2 classes C6 and U5 is about average, with U5 ($\beta_B^{(3.0,14)} = 0.67$) looking slightly better than C6.

When the level 3 class {C6, U5} is formed, homogeneity drops remarkably ($\beta_B^{(3.0,14)} = 0.1504$). Since the off-diagonal rectangular blocks of the scattergram have small values, one deduces that cross-correlation between C6 and U5 is low. In other words, image analysis has detected differences in morphology caused by the template even if the sample was not spatially homogeneous.

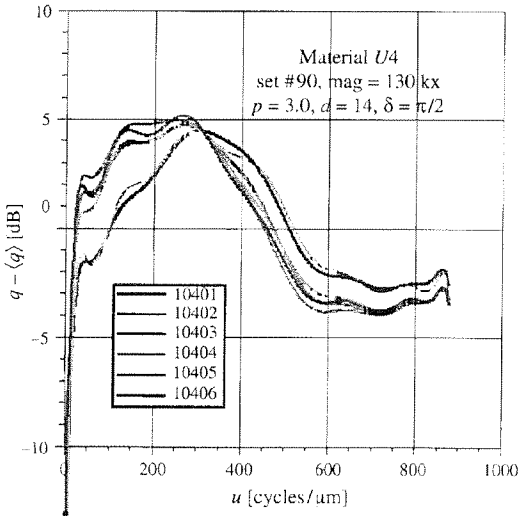

Fig. 13. Mean removed polynomials of level 1 class U4. Set 90. Different tiles less than 500 nm apart have different morphology. The corresponding block in Figure 10 is $25 \leq i, j \leq 30$. The two polynomials which grow more slowly and decay at a higher u give rise to the dark stripes at $i = 25$ and $i = 28$ in Figure 10.

In all cases there are U tiles which correlate better with C tiles than with those in their own level 1 class.

Set 40 at $\hat{p} = 2.7$ behaves similarly.

IS = 4 and 2

Column 4 of Table V suggests that growth on a template yielded a definitely more uniform material when IS = 4 and a slightly more uniform one when IS = 2.

IS = 1

Homogeneity of (level 2) classes {C5, C6} and U5 is low, with U5 looking slightly more homogeneous ($\beta_B^{(2.7,14)} = 0.4921$) than {C5, C6} ($\beta_B^{(2.7,14)} = 0.485$). However, the level 3 class indicator $\beta_B^{(2.7,14)}$ drops to 0.39 (column 5 of Table V). Once again the coated and uncoated materials must have different morphology.

5.4. Univariate Statistics of Set 90

Further classification of set 90 was made possible by type 2 image descriptors. Classification is of univariate type, because one descriptor at a time was used. The link between type 1 and type 2 descriptors can be inferred from Figures 12 and 13. Plots of interpolating polynomials typically exhibit a sharp rise, one or more local maxima, a smooth rolloff, and a local minimum occurring before $u = 600\ \mu\text{m}^{-1}$. Since $p = 3.0$ and $d = 14$, these superscripts are dropped throughout.

The following type 2 descriptors were found to be significant:

- M, the abscissa of the highest local maximum
- $q[M]$, the corresponding ordinate
- m, the abscissa of the lowest local minimum in $0 \leq u \leq (3/4)u_{\max}$
- $q[m]$, the corresponding ordinate
- s, the abscissa of minimum slope in $0 \leq u \leq (3/4)u_{\max}$
- $q'[s]$, the derivative of $q[\cdot]$ at s
- $A = \int_E (q[u] - q[m])\, du$, where E is the interval $\subset [0, m]$ within which $q[u] - q[m] \geq 0$, hence A is the area under the bell
- $C = \int_F (q[u] - q[s])\, du$, where F is the interval $\subset [0, s]$ within which $q[u] - q[s] \geq 0$, hence C is the area under the peak.

Since all the analyzed polynomials comply with $s < m$, then $C < A$. Oscillations and other features of the polynomials occurring at frequencies higher than 600 μm^{-1} are interpolation artifacts and were ignored.

The most remarkable results have been summarized by scattergrams of M vs s (Fig. 14) and A vs C (Fig. 15). In order to improve readability, each level 1 class (6 tiles) has been replaced by its centroid, the coordinates of which are the arithmetic averages of the given indicators over the 6 tiles. Centroid labeling is obvious.

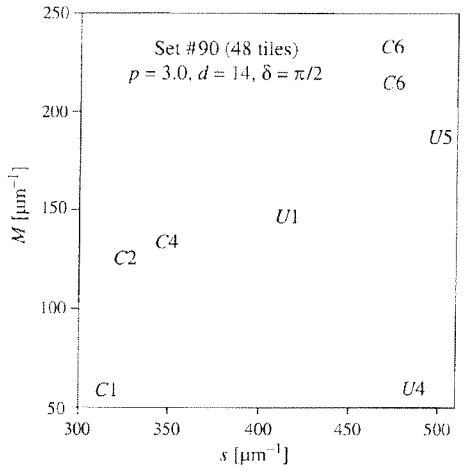

Fig. 14. Scattergram of class centroids of set 90 in the $\{s, M\}$ plane. M = abscissa of highest local maximum. s = abscissa of minimum slope in $0 \le u \le (3/4)u_{max}$. Each centroid is denoted by the class label. Very roughly, materials could be classified into three groups by means of s alone, because the abscissas of {C1, C2, C4} separate from those of {C6, U4, U5} and U1.

In Figure 14, with reference to s, materials can be divided into 3 clusters: {C1, C2, C4} such that $300 \le s \le 400\ \mu m^{-1}$, {C6 (two sets of 6 tiles), U4, U5} such that $440 \le s \le 540$ and U1, a singleton, the tiles of which exhibit a wider spread. In other words, s alone could serve as a coarse morphological classifier.

In Figure 15, classes {C1, C2, C4} form a cluster bound by the rectangle $\{500 < C < 1000\ dB/\mu m\} \times \{3000 < A < 4000\ dB/\mu m\}$.

All remaining material classes lie below the straight line $A = C + 2000$, the diagonal of the displayed square.

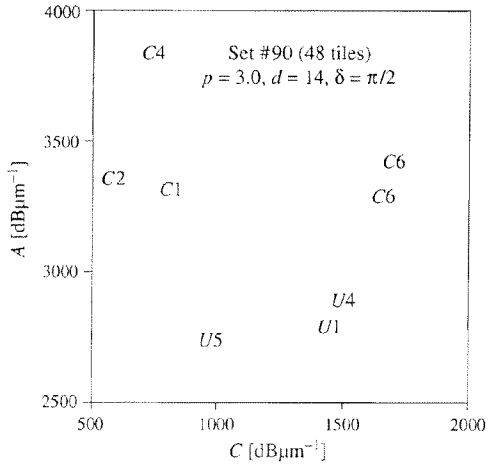

Fig. 15. Scattergram of class centroids of set 90 in the {C, A} plane. C = area under the peak, A = area under the bell. Once again, materials {C1, C2, C4} form a cluster, bound by the rectangle on the top left $\{500 < C < 1000\ dB/\mu m\} \times \{3000 < A < 4000\ dB/\mu m\}$. All remaining material classes lie below the diagonal of the displayed square.

The physical interpretation of all results, whether from multivariate (Sections 5.1–5.3) or univariate (Section 5.4) analysis, is provided by the next section.

6. DISCUSSION AND PHYSICAL INTERPRETATION

As explained in Sections 4.2 and 4.3, to each TEM image (j) there corresponds a polynomial $q_j^{(p,d)}[\cdot]$, which in turn depends on the parameters p and d. Multivariate statistical analysis (Sections 5.1–5.3) has processed information carried by polynomials as a whole. Comparison between individual images (level 1) or materials (levels 2 and 3) has been made possible by the correlation matrix $\boldsymbol{R}^{(p,d)}$.

The first relevant finding is the existence of a model exponent $\hat{p}$ (Section 5.1) about which interclass homogeneity $\mu^{(\hat{p},14)}$ is stationary. In physical terms, by choosing $\hat{p}$, morphological analysis is least affected by a parameter of the algorithm and mostly controlled by material properties.

Sections 5.2 and 5.3 have provided a quantitative assessment of spatial uniformity and of the role of the template and supported the qualitative judgment derived from visual observation at the TEM.

Univariate statistics, i.e., the analysis of the indicators listed in Section 5.4 and taken one-by-one, has provided further insight into size and shape of nanoparticles and their aggregates. This claim is supported by the following arguments.

Very roughly speaking the raw enhanced spectrum $h[\cdot]$, and consequently the polynomial $q[\cdot]$, in the interval $0 \le u \le 255$ cycles/image (420 μm^{-1} at 130 k× and 960 μm^{-1} at 280 k×) describes image "structure," whereas $255 < u \le u_{max}$ corresponds to "texture." The distinction between image structure (coarse scale) and texture (fine scale) is a fundamental paradigm in image analysis.[11] Wherever $h[\cdot] > 0$, the power spectral density of the image decays more slowly than that of the model, hence the material has significant micro- or nanostructure.

By very simple arguments of Fourier analysis, one could show that the height $(q[M])$ of the positive peak of either $h[\cdot]$ or $q[\cdot]$ and its width (s) are affected by particle size distribution and particle edge sharpness. If particles sizes vary in a narrow range, then $q[M]$ is high, s is small, and the slope $q'[s]$ is steep (negative and large in magnitude). Moreover, for a given area A under the bell, a smaller value of C suggests that the positive peak of $q[\cdot]$ is relatively narrow. Materials C1, C2, and C4 do satisfy these conditions. In particular, $100 \le M \le 200\ \mu m^{-1}$ may suggest that particle sizes range from 2.5 to 5 nm, with a maximum at 3.3 nm. Instead, a broad size distribution lowers $q[M]$ and makes $q[\cdot]$ decay more slowly. As a consequence the area under the peak itself, C, becomes larger as compared to A, although the inequality $C < A$ is always met. This is the case for materials C6, U1, U4, U5. For

Table VI. Relative intensity of rings in the selected area diffraction patterns.

IS	Materials	Ring intensity
1	C5, C6	2, 0
	U5	0
2	C4	4
	U4	1
3	C3	4
	U3	2
4	C1, C2	2, 1
	U1, U2	0, 0

0 = not visible; 4 = neatly visible.

example, the maxima of U4 occur in $250 \leq u \leq 320\ \mu m^{-1}$ and on average are 10 dB lower than those of C4. Hence particle sizes have a broader distribution. In fact, some tiles exhibit up to three local maxima. Material C6, the size distribution of which peaks at 2 nm, cannot be told apart from the U materials.

Information about the crystal structure of the materials was obtained by SADP. The intensity of diffraction rings was qualitatively ranked from 0 to 4 (maximum visibility) and Table VI was compiled accordingly. Relatively high ring intensities of C1, C2, and C4 patterns correlate with the sharper peaks of $q[\cdot]$ (Figs. 12 and 14) and their centroid coordinates in Figure 15. Similarly, the morphological indicators of C6, U1, and U5 correlate with the absence of a crystal structure. In the case of C6 one may infer that IS = 1 may have been inadequate to achieve both spatial uniformity of the aggregates and reproducibility of the result.

7. CONCLUSION

Nanosized aluminum silicate particles have been produced via mineralization from solution at near room temperature on a self-assembled organic multilayer template.

Some experimental control parameters have been deliberately varied and the role of each has been assessed.

The nanomaterials have been characterized by analytical transmission electron microscopy and electron diffraction. Fourier analysis of *TEM* images and "spectrum enhancement" have provided quantitative morphological indicators, by which the spatial uniformity of nanoparticle distribution and the role of the template have been assessed.

Univariate and multivariate statistics have allowed classification of the materials. The key step has been the selection of the model exponent p, which solves a saddle point problem: maximization of interclass heterogeneity and minimization of intraclass heterogeneity (Section 5.1). Multivariate results have been summarized by the correlation matrix $R^{(p,d)}$ of interpolating polynomials $(q[\cdot])$. Some morphological indicators extracted from the $q[\cdot]$s have been further related to the physical properties of the nanoparticles and their aggregates.

Higher precursor concentration resulted in a higher degree of crystallinity (Fig. 3). High [Si]:[Al] yielded crystalline aluminum silicate.

The area density and uniformity of particles were dramatically increased by the presence of the multilayer polymer film template (A vs B in Fig. 2, Fig. 4). More precisely, mineralization on a template with IS = 2 or 4 yielded good results in terms of uniformity of nanoparticle size (Section 6), sharpness of nanoparticle boundaries (Section 6), and spatial uniformity of the deposit (Section 5.2). The first two features correlate with crystal structure (Table VI). Instead, mineralization with IS = 1 performed poorly, the morphology of the corresponding materials was insensitive to the presence of a template.

Although the set of analyzed images was relatively small, the conclusions drawn from quantitative morphology are self-consistent and agree with the results of electron diffraction. A proof of principle has been given of a new classification method based on spectrum enhancement followed by statistical analysis.

On the applications side, the above findings can provide feedback to control the fabrication process.

On the physical modeling side, quantitative morphology may have a role in understanding the mineralization mechanism, which certainly involves phase separation, percolation-cluster transitions, and other phenomena, as suggested, e.g., by Ref. 12.

Acknowledgment: G. F. Crosta acknowledges the partial financial support of Fondo di Ateneo per la Ricerca (FAR) 2002, 2003, and 2004, granted by Università degli Studi Milan-Bicocca, Milan, Italy.

References and Notes

1. A. Ulman, *Characterization of Organic Thin Films*, Butterworth-Heinemann, Boston, MA (**1995**).
2. A. Ulman, *Introduction to Ultrathin Organic Films*, Academic Press, Boston, MA (**1999**).
3. J. Liu, A. Y. Kim, L. Q. Wang, B. J. Palmer, Y. L. Chen, P. Bruinsma, B. C. Bunker, G. J. Exarhos, G. L. Graff, and P. C. Rieke, *Adv. Colloid Interface Sci.* 69, 131 (**1996**).
4. V. Tsukruk, *Prog. Polym. Sci.* 22, 247 (**1997**).
5. N. C. Beck Tan, L. Balogh, S. F. Trevino, D. A. Tomalia, and J. S. Lin, *J. Polym.* 40, 2535 (**1999**).
6. B. Kang, P. J. Stenhouse, G. F. Crosta, and C. Sung, *Korean-American Scientists and Engineers Association Letters 2002*.
7. J. C. Huling and G. L. Messing, *J. Am. Ceram. Soc.* 74, 2374 (**1991**).
8. G. F. Crosta, C. Urani, and L. Fumarola, "Fourier and fractal analysis of cytoskeletal morphology altered by xenobiotics", in *Proceedings of the SPIE, Manipulation and Analysis of Biomolecules, Cells and Tissues*, edited by D. V. Nicolau, J. Enderlein, R. C. Leif, and D. Farkas, SPIE, Bellingham, WA (**2003**), Vol. 4962, pp. 329–340.
9. G. F. Crosta, S. Zomer, S. Holler, Y.-L. Pan, and C. Sung, "Classification and Recognition of Limited Aperture Scattered Intensity Patterns from *TAOS* Experiments," in *Progress in Electromagnetic*

Research Symposium 2003 Proceedings, edited by J. Au Kong et al., Electromagnetics Academy, Cambridge, MA (**2003**), p. 507.
10. W. H. Press, S. A. Teukolsky, W. T. Vetterling, and B. P. Flannery, *Numerical Recipes in C—The Art of Scientific Computing*, 2nd ed., Cambridge University Press, Cambridge, UK (**1992**).
11. Y. Meyer, *Oscillating Patterns in Image Processing and Nonlinear Evolution Equations—The Fifteenth Dean Jacqueline B. Lewis Memorial Lectures*, AMS, Providence, RI (**2001**).
12. K. Nakanishi and N. Soga, *J. Am. Ceram. Soc.* 74, 2518 (**1991**).

Received: 10 February 2004. Accepted: 15 May 2004.